

Explainable Classifier for Malignant Lymphoma Subtyping via Cell Graph and Image Fusion

Daiki Nishiyama^{1,2}, Hiroaki Miyoshi³, Noriaki Hashimoto², Koichi Ohshima³, Hidekata Hontani⁴, Ichiro Takeuchi^{5,2}, and Jun Sakuma^{1,2}

¹ Institute of Science Tokyo, Tokyo, Japan

nishiyama.d.2d7f@m.isct.ac.jp

² RIKEN AIP, Tokyo, Japan

³ Kurume University, Fukuoka, Japan

⁴ Nagoya Institute of Technology, Aichi, Japan

⁵ Nagoya University, Aichi, Japan

Abstract. Malignant lymphoma subtype classification directly impacts treatment strategies and patient outcomes, necessitating classification models that achieve both high accuracy and sufficient explainability. This study proposes a novel explainable Multi-Instance Learning (MIL) framework that identifies subtype-specific Regions of Interest (ROIs) from Whole Slide Images (WSIs) while integrating cell distribution characteristics and image information. Our framework simultaneously addresses three objectives: (1) indicating appropriate ROIs for each subtype, (2) explaining the frequency and spatial distribution of characteristic cell types, and (3) achieving high-accuracy subtyping by leveraging both image and cell-distribution modalities. The proposed method fuses cell graph and image features extracted from each patch in the WSI using a Mixture-of-Experts (MoE) approach and classifies subtypes within an MIL framework. Experiments on a dataset of 1,233 WSIs demonstrate that our approach achieves state-of-the-art accuracy among ten comparative methods and provides region-level and cell-level explanations that align with a pathologist’s perspectives.

Keywords: Explainable AI · Multimodality · Multiple Instance Learning · Malignant Lymphoma · Subtyping · Whole Slide Image · Cell Graph

1 Introduction

Subtyping of malignant lymphomas directly impacts patient prognosis and is essential for determining appropriate treatment strategies. Recent advances in whole slide imaging (WSI) technology [2,15,31] have made it possible to develop machine learning models capable of classifying malignant lymphoma subtypes from WSI. However, for the model to be successfully integrated into clinical practice, it must not only achieve high diagnostic accuracy but also provide a reliable explanation for its decisions.

Approaches that mimic the diagnostic processes employed by pathologists are viewed as beneficial for attaining high classification accuracy and reliable explanations. Pathologists diagnose lymphoma subtypes by investigating H&E-stained

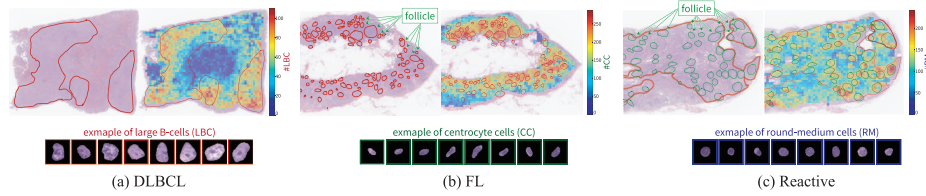


Fig. 1. Left to right: DLBCL, FL, and Reactive case, and cells characteristic of each subtype (DLBCL corresponds to LBC, FL to CC, and Reactive to RM). Red lines indicate ROIs, and green and red lines in Reactive and FL, respectively, indicate follicles. Heat maps indicate the spatial distribution of the number of cells characteristic of each subtype in a 512-pixel square at 40x magnification.

slide specimens. They concentrate on local regions of interest (ROIs), which vary for each subtype, and analyze the characteristics, frequency, and spatial distribution of each cell type within these ROIs. During diagnosis, pathologists utilize not only cell-based features but also visual information from pathological images to understand the broader tissue architecture.

As examples, we explain using three clinically important subtypes that we address in this research: diffuse large B-cell lymphoma (DLBCL), follicular lymphoma (FL), and reactive lymphoid hyperplasia (Reactive). Figure 1 shows, for each subtype, a representative case along with its ROIs, cells corresponding to the subtype, and the distribution of these cells’ counts across the WSI. ROIs of DLBCL show a high frequency of large B-cells (LBCs). ROIs of FL are inside of nearly round structures called *follicles*, where an overabundance of certain cell types such as centrocytes (CCs). ROIs of Reactive extend between the follicles and between them, and many round-medium cells (RMs) are observed, especially near the boundaries of follicles. As Fig. 1 indicates, the distribution of cell types characteristic to each subtype is observed only when ROIs specific to that subtype can be properly determined.

Consequently, an explainable malignant lymphoma classification model must be able to (1) identify appropriate ROIs for each subtype, (2) explain the frequency and spatial distribution of characteristic cell types, and (3) achieve high-accuracy subtyping by leveraging both image and cell distribution modalities. Cell-level explanations (2) rely on accurately identifying subtype-specific ROIs (1), while the correct determination of ROIs is contingent on understanding cell-type distributions and sustaining overall classification accuracy (3). Therefore, our goal is to integrate all three capabilities simultaneously and accomplish a reliable and explainable subtype classification of malignant lymphomas.

1.1 Related Works

WSI is gigapixel-scale images that cannot be directly processed by machine learning due to memory constraints. Multiple Instance Learning (MIL) [12,23] addresses this by partitioning WSIs into a set (called *bag*) of smaller patches

(called *instances*). To indicate ROIs in a WSI, attention-based MILs (ABMILs) [18,29,32] highlight important regions but provide only a single attention score. This is insufficient for lymphoma subtyping, where different regions are important for different subtypes. AdditiveMIL [20] can be a solution to this situation by providing attention scores of instances for each subtype, clarifying the contribution of each instance to the subtyping result. One limitation of these is that they rely solely on image features without explicitly utilizing cell information.

Cell graphs, where nodes represent cells and edges denote cell adjacencies, effectively capture spatial cell distributions in pathological images [4,5]. They can be transformed into feature vectors by graph neural networks (GNNs) to classify subtypes and grades investigated in [1,3,14,19,22,25,28,30,34]. For instance, HACT-Net [28] introduced hierarchy into cell graphs to deal with cell-level and tissue-level graph structure. A method to quantitatively explain morphological cell attributes, such as size, shape, and chrominance, was proposed in [19]. However, these methods are designed for pre-defined, small-scale ROI rather than WSI-scale, limiting their ability to (1) discover local ROIs specific to the assumed subtype in WSI and (2) utilize cell graphs in the discovered ROIs for subtyping. These limitations are interdependent in malignant lymphoma subtyping and cannot be solved by a simple application of existing methods.

1.2 Contributions

To resolve these problems, multimodal MIL-based models that utilize both image and cell graphs are seen as effective. Our contributions are summarized as follows:

- We propose an explainable classification framework for malignant lymphoma WSI that indicates localized ROIs through class-wise importance per patch and demonstrates the frequency and spatial distribution of characteristic cell types. Experiments confirm that our framework provides region- and cell-level explanations well aligned with pathologists’ views.
- To achieve high accuracy, our framework fuses cell graph and image features in a mixture-of-expert (MoE) manner within a MIL framework. Our method achieves state-of-the-art accuracy among ten comparison methods in classifying three major lymphoma subtypes in a 1,233 WSI dataset.
- According to our investigation, 16 computational pathology studies utilize cell graphs, yet none of them address malignant lymphoma. Our work is, therefore, the first to apply cell graphs specifically to malignant lymphoma.

2 Methodology

We treat each WSI of lymph node tissue as a *bag* comprising multiple *instances* (patches). Let $n \in \{1, \dots, N\}$ be an index of bags (WSIs), $m \in \{1, \dots, M\}$ an index of instances in a bag, $X_{n,m}$ be the m -th image instance in the n -th bag, and $\mathbf{y}_n \in \{0, 1\}^K$ be the n -th one-hot label over the $K = 3$ subtypes, i.e., DLBCL, FL, and Reactive. Here, we define $\mathbb{X}_n = \{X_{n,m}\}_{m=1}^M \in \mathcal{X}$ as the n -th image bag, where \mathcal{X} is a space of image bags. Then the n -th bag is defined by $\mathcal{B}_n = (\mathbb{X}_n, \mathbf{y}_n)$.

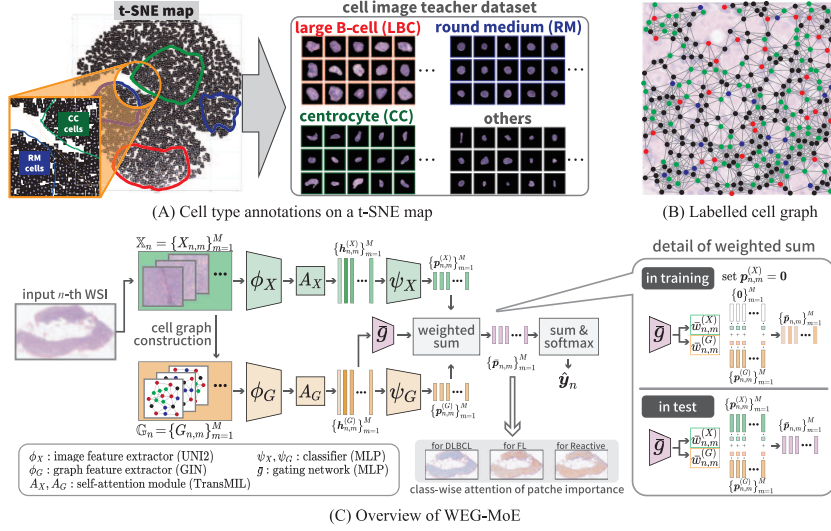


Fig. 2. (A) Annotations on a t-SNE map to label cells with LBC, CC, RM, or others. (B) Example of a cell graph to be constructed. The nodes’ color indicates the cell type. (C) An overview of our method, WEG-MoE, for classifying the n -th WSI.

2.1 Labeled Cell Graph Construction

We construct a labeled cell graph $G_{n,m}$ with cells contained in $X_{n,m}$, where a node label representing a cell type is given to each corresponding node. For cell labeling, we combine cell segmentation using HoVerNet [13] pre-trained on CoNsep [13] with a cell-type classifier. As Figure 2(A) shows, we create training data by detecting cells in $X_{n,m}$, encoding them with pre-trained ResNet34 [11], projecting onto a 2D t-SNE space, and having a pathologist label cell types: LBC, CC, RM, and others. Identifying LBC, CC, and RM with high recall is crucial for lymphoma subtyping. Thus, we employed CAMRI loss [26,27] as the loss function, which enables the classifier to maintain relatively high recall for these three classes while preserving overall accuracy.

Finally, we get the labeled cell graph $G_{n,m} = (V_{n,m}, E_{n,m}, L_{n,m})$ corresponding to $X_{n,m}$ like Fig. 2(B), where $V_{n,m}$ is the set of cell indices, $E_{n,m}$ is the set of edges connecting cells within radius r to reflect the spatial density of cells ($r = 60$ in our setting), and $L_{n,m}$ is the set of corresponding cell labels. Let $\mathbb{G}_n = \{G_{n,m}\}_{m=1}^M$, then we formulate the n -th WSI bag by $\mathcal{B}_n = (\mathbb{X}_n, \mathbb{G}_n, \mathbf{y}_n)$.

2.2 MoE-based Multimodal MIL

As we stated in Sec. 1, the frequency and spatial distribution of specific cell types are crucial for lymphoma subtyping. While labeled cell graphs provide this information, they lack visual elements like cell texture and tissue architecture

found in pathological images. Therefore, combining cell graphs with image features is essential for accurate and explainable subtyping. Therefore, for an input $\mathcal{B}_n = (\mathbb{X}_n, \mathbb{G}_n, \mathbf{y}_n)$, we develop an explainable multimodal classification model utilizing both images and graphs to achieve high classification performance.

Pretraining AdditiveMIL for Two Modality. To capture RoI with different features for each subtype, as we stated in Sec. 1, we adopt AdditiveMIL [20]. We first introduce AdditiveMIL, where only a single modality (cell graph or image patch) is available. Let f_G and f_X be MIL models for cell graphs and images, respectively, $\phi_G: \mathcal{G} \rightarrow \mathbb{R}^d$ be a feature extractor (e.g., GIN [33]) of f_G , and $\phi_X: \mathcal{X} \rightarrow \mathbb{R}^d$ be a feature extractor (e.g., UNI [7]) of f_X . Given an instance $(X_{n,m}, G_{n,m})$ in a bag \mathcal{B}_n , these models produce d -dimensional latent features:

$$\mathbf{h}_{n,m}^{(G)} = A_G(\phi_G(G_{n,1}), \dots, \phi_G(G_{n,M}))_m, \mathbf{h}_{n,m}^{(X)} = A_X(\phi_X(X_{n,1}), \dots, \phi_X(X_{n,M}))_m, \quad (1)$$

where $A_G, A_X: \mathbb{R}^{M \times d} \rightarrow \mathbb{R}^{M \times d}$ are self-attention modules (e.g., TransMIL [29]). We obtain the bag-level class probability after each $\mathbf{h}_{n,m}^{(\cdot)}$ is mapped to a K -dimensional logit via $\psi_G, \psi_X: \mathbb{R}^d \rightarrow \mathbb{R}^K$, which are learnable functions (e.g., multilayer perceptrons (MLPs)):

$$\begin{aligned} \mathbf{p}_{n,m}^{(G)} &= \psi_G(\mathbf{h}_{n,m}^{(G)}), & \mathbf{p}_{n,m}^{(X)} &= \psi_X(\mathbf{h}_{n,m}^{(X)}), & (2) \\ \hat{\mathbf{y}}_n^{(G)} &= \text{softmax}\left(\sum_{m=1}^M \sigma(\mathbf{p}_{n,m}^{(G)})\right), & \hat{\mathbf{y}}_n^{(X)} &= \text{softmax}\left(\sum_{m=1}^M \sigma(\mathbf{p}_{n,m}^{(X)})\right), & (3) \end{aligned}$$

where σ is a sigmoid function to stabilize learning in our case (optional), and softmax is a softmax function. Here, the j -th element of $\mathbf{p}_{n,m}^{(\cdot)}$ represents the importance of the m -th instance, assuming the prediction result is the j -th class. Because $\hat{\mathbf{y}}_n^{(\cdot)}$ is given as an addition of the class-wise attention score $\mathbf{p}_{n,m}^{(\cdot)}$, the impact of each instance on the classification can be obtained for each class. f_G and f_X are pre-trained independently using cross-entropy loss $\ell(\hat{\mathbf{y}}_n^{(\cdot)}, \mathbf{y}_n)$.

Weak-Expert-based Gating MoE. To combine image and cell graph experts, we employ a MoE-based approach. First, we introduce a naive MoE. Let $g: \mathbb{R}^{2d} \rightarrow [0, 1]^2$ be a gating function that estimates how much to rely on each modality expert in the mixture. Then, the bag-level prediction by MoE is given by

$$\hat{\mathbf{y}}_n^{(\text{moe})} = \text{softmax}\left(\sum_{m=1}^M w_{n,m}^{(G)} \mathbf{p}_{n,m}^{(G)} + w_{n,m}^{(X)} \mathbf{p}_{n,m}^{(X)}\right), \quad (4)$$

$$[w_{n,m}^{(G)}, w_{n,m}^{(X)}] = \text{softmax}(g(\text{cat}[\mathbf{h}_{n,m}^{(G)}, \mathbf{h}_{n,m}^{(X)}])), \quad (5)$$

where cat is a concatenate of vectors. Each $w_{n,m}^{(\cdot)}$ in Eq. (5) can be interpreted as how much each modality contributes to the m -th instance in the n -th bag. The gating mechanism g allows the model to combine graph-based and image-based features adaptively, considering the contributions of both modalities.

Table 1 shows that unimodal of either image (ResNet50, UNI2) or graph (GIN) alone yields decent classification performance. However, a naive MoE

combination (UNI2, GIN) tends to ignore graph-based experts, possibly because image features achieve loss minimization more rapidly. To better utilize both modalities while preserving explainability, we propose Weak-Expert-based Gating MoE (WEG-MoE), shown in Fig. 2(C). This approach trains the gating function using only graph features $\mathbf{h}_{n,m}^{(G)}$, which typically have lower classification accuracy. The bag-level prediction by WEG-MoE is given by:

$$\hat{\mathbf{y}}_n^{(\text{weg})} = \text{softmax}\left(\sum_{m=1}^M \bar{w}_{n,m}^{(G)} \mathbf{p}_{n,m}^{(G)} + \bar{w}_{n,m}^{(X)} \mathbf{p}_{n,m}^{(X)}\right), \quad (6)$$

$$\text{where } [\bar{w}_{n,m}^{(G)}, \bar{w}_{n,m}^{(X)}] = \text{softmax}(\bar{g}(\mathbf{h}_{n,m}^{(G)})). \quad (7)$$

By forcing $\mathbf{p}_{n,m}^{(X)} = \mathbf{0}$ during training and optimizing only \bar{g} 's parameters, WEG-MoE learns to judge where graph-based features are useful, switching to image-based experts when necessary.

In Sec. 3, we demonstrate high classification performance achieved by WEG-MoE and the validity of explanations by the class-wise attention and cell graph.

3 Experiments

3.1 Experiment Setup

We used a private dataset comprising 1,233 WSIs (411 per subtype) from lymph node tumors, obtained with an Aperio GT 450 at 40x magnification, collected at Kurume University. The cell classifier was trained on 237,544 cell images carefully selected to prevent test data leakage. Each patch was clipped at 512×512 pixels from a non-background area and selected if it had at least 100 cells.

Our model, WEG-MoE, uses UNI2 [7] followed by a fully connected layer for ϕ_X , and a four-layer GIN [33] for ϕ_G . During pre-training, only non-UNI2 weights were optimized for f_X , while the entire f_G was optimized. We used three-layer MLPs with ReLU for ψ_X , ψ_G , and \bar{g} , with latent dimension $d=256$. For comparison, we implemented unimodal baselines: ResNet50 [17], UNI2 [7], GIN [33], and HACT-Net [28] adapted for MIL, and multimodal approaches fusing $\mathbf{h}_{n,m}^{(X)}$ and $\mathbf{h}_{n,m}^{(G)}$ in Eq. (1): concat [24], Pathomic Fusion [8], MCAT [9], mutual attention [6], and MoE [16]. HACT-Net utilizes deep features for node features and a PNA [10] for the GNN. Pathomic Fusion fused by a direct product after reducing their dimension to 48. In MCAT, we employed both one-directional attention flows from graphs/images to images/graphs (g2i and i2g). Mutual attention performs cross-attention between images and graphs. All predictions used AdditiveMIL [20] and TransMIL [29] as self-attention mechanisms for A_X and A_G . Adam [21] optimised these models. Our implementation is publicly available⁶.

3.2 Results

Table 1 presents classification results on the test folds of five-fold cross-validation. As we can see, our method, WEG-MoE, outperforms the other approaches in classification performance.

⁶ <https://anonymous.4open.science/r/WEG-MoE-B9B3>

Table 1. The mean and standard deviation of the accuracy, AUC for each class, and mean AUC for each class in the five validation sets. The table is divided into sections of image, cell graph, and multimodal by lines from the top. The best performances for each metric are indicated in bold.

Method	Accuracy	DLBCL AUC	FL AUC	Reactive AUC	AUC mean
ResNet50[17]	0.842 ± 0.032	0.956 ± 0.022	0.870 ± 0.059	0.973 ± 0.016	0.933 ± 0.045
UNI2[7]	0.904 ± 0.014	0.980 ± 0.010	0.948 ± 0.015	0.988 ± 0.010	0.972 ± 0.017
GIN[33]	0.829 ± 0.019	0.964 ± 0.012	0.807 ± 0.047	0.916 ± 0.025	0.896 ± 0.065
HACT-Net[28]	0.761 ± 0.077	0.957 ± 0.022	0.856 ± 0.045	0.943 ± 0.023	0.919 ± 0.045
concat[24]	0.907 ± 0.012	0.980 ± 0.011	0.954 ± 0.002	0.989 ± 0.008	0.975 ± 0.015
Pathomic Fusion[8]	0.902 ± 0.015	0.975 ± 0.017	0.949 ± 0.016	0.986 ± 0.012	0.970 ± 0.015
MCAT g2i[9]	0.901 ± 0.011	0.973 ± 0.010	0.953 ± 0.013	0.988 ± 0.004	0.971 ± 0.014
MCAT i2g[9]	0.881 ± 0.019	0.975 ± 0.013	0.951 ± 0.015	0.986 ± 0.006	0.971 ± 0.015
mutual attention[6]	0.906 ± 0.018	0.972 ± 0.017	0.956 ± 0.008	0.987 ± 0.007	0.972 ± 0.013
MoE[16]	0.907 ± 0.012	0.977 ± 0.013	0.951 ± 0.016	0.988 ± 0.010	0.972 ± 0.015
WEG-MoE (ours)	0.911 ± 0.011	0.983 ± 0.009	0.961 ± 0.011	0.988 ± 0.010	0.977 ± 0.012

Figure 3 shows explainability results with a representative case: (A) class-wise attention of each subtype, (B) frequency by cell type, and (C) frequency of cell adjacency. (B) and (C) are computed from high-attention regions (top 25%). Dotted lines show distribution within pathologist-supervised ROIs. Below, we contrast what the pathologist expects with explanations by the model.

DLBCL. Expectation: DLBCL has widely spread lesions with increased and diffusely distributed LBC. **Attention:** Figure 3(A-1) shows higher attention for DLBCL overall than other subtypes, which reflects the fact that LBC is diffusely distributed overall. **Cell frequency:** Figure 3(B-1) indicates increased LBCs compared to other subtypes. **Cell distribution:** LBCs in DLBCL (Fig. 3(C-1)) are adjacent to a greater variety of cells than in Reactive (Fig. 3(C-2)). **Validity** These findings are consistent with the expected distribution of LBC in lesions and are also close to the distribution in the ROI, so they are aligned with the pathologist’s view.

FL. Expectation: FL lesions are follicles with densely packed cells and numerous CCs. **Attention:** Figure 3(A-2) shows higher attention for FL in localized regions, while lower for Reactive and DLBCL. **Cell frequency:** Figure 3(B-2) indicates increased CCs compared to other subtypes. **Cell distribution:** The number of CCs adjacent to various cells in FL (Fig. 3(C-3)) exceed those in Reactive (Fig. 3(C-4)). **Validity:** These results indicate that the follicles show attention and that these follicles have the characteristics of FL rather than Reactive, so they are aligned with the pathologist’s view.

Reactive. Expectation: Reactive tissue shows normal follicular structure and interfollicular tissue throughout, with RM often at follicle boundaries. **Attention:** Figure 3(A-3) shows high attention for Reactive overall, with locally high FL attention in the lower part. **Cell frequency:** Reactive shows fewer LBCs than DLBCL ((B-3) vs (B-1)) and fewer CCs, RMs, and other cells than FL ((B-3) vs (B-2)). **Cell distribution:** Reactive shows fewer cell adjacencies for both LBCs and CCs compared to DLBCL and FL, respectively. **Validity:** Areas

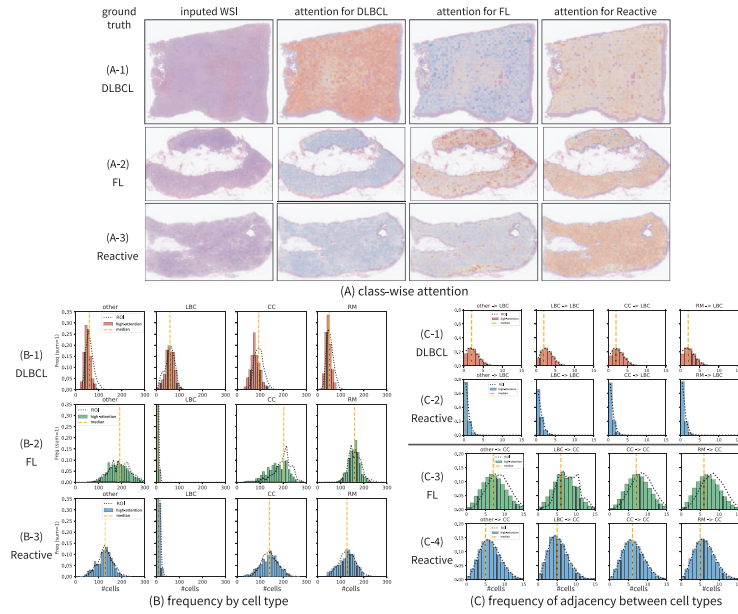


Fig. 3. (A) Class-wise attention, where higher attention is red, and lower is blue. (B) Frequency by cell types. (C) Frequency of adjacency between cell types. In (B) and (C), the black dotted lines present the results computed with the ROI supervised by a pathologist, which can be interpreted as the ground truth, and the orange dotted lines present the median of the distribution. In (C), for example, “LBC→CC” indicates the number of CCs that are connected by edges to LBC. Each data in (B) and (C) is from the top 25% of instance-level class-wise attention scores for the correct class.

with high FL attention appear as FL to pathologists, while other regions display Reactive characteristics rather than malignant patterns, validating the model’s attention allocation. The Reactive regions both inside and outside follicles did not show elevated RM frequency at follicular borders as might be expected. When comparing cell distributions, the Reactive case displays non-malignant patterns distinct from DLBCL and FL. These patterns closely match the distribution in pathologist-identified ROIs, confirming the overall appropriateness of the model’s interpretations.

4 Conclusion

We proposed an explainable multimodal MIL framework for the subtyping of malignant lymphoma. This framework can explain not only localized ROIs through class-wise attention but also the frequency and spatial distribution of characteristic cell types based on the labeled cell graph. Our experiments confirmed, via the pathologist’s assessments, the appropriateness of these explanations and demonstrated superior classification performance compared to related methods.

References

1. Abbas, S.F., Le Vuong, T.T., Kim, K., Song, B., Kwak, J.T.: Multi-cell type and multi-level graph aggregation network for cancer grading in pathology images. *Medical Image Analysis* **90**, 102936 (2023)
2. Afonso, M., Bhawsar, P.M., Saha, M., Almeida, J.S., Oliveira, A.L.: Multiple instance learning for wsi: A comparative analysis of attention-based approaches. *Journal of Pathology Informatics* **15**, 100403 (2024)
3. Baranwal, M., Krishnan, S., Oneka, M., Frankel, T., Rao, A.: Cgat: Cell graph attention network for grading of pancreatic disease histology images. *Frontiers in Immunology* **12**, 727610 (2021)
4. Bilgin, C., Demir, C., Nagi, C., Yener, B.: Cell-graph mining for breast tissue modeling and classification. In: 2007 29th Annual international conference of the IEEE Engineering in Medicine and Biology Society. pp. 5311–5314. IEEE (2007)
5. Brussee, S., Buzzanca, G., Schrader, A.M., Kers, J.: Graph neural networks in histopathology: Emerging trends and future directions. *Medical Image Analysis* p. 103444 (2025)
6. Cai, G., Zhu, Y., Wu, Y., Jiang, X., Ye, J., Yang, D.: A multimodal transformer to fuse images and metadata for skin disease classification. *The Visual Computer* **39**(7), 2781–2793 (2023)
7. Chen, R.J., Ding, T., Lu, M.Y., Williamson, D.F., Jaume, G., Chen, B., Zhang, A., Shao, D., Song, A.H., Shaban, M., et al.: Towards a general-purpose foundation model for computational pathology. *Nature Medicine* (2024)
8. Chen, R.J., Lu, M.Y., Wang, J., Williamson, D.F., Rodig, S.J., Lindeman, N.I., Mahmood, F.: Pathomic fusion: an integrated framework for fusing histopathology and genomic features for cancer diagnosis and prognosis. *IEEE Transactions on Medical Imaging* (2020)
9. Chen, R.J., Lu, M.Y., Weng, W.H., Chen, T.Y., Williamson, D.F., Manz, T., Shady, M., Mahmood, F.: Multimodal co-attention transformer for survival prediction in gigapixel whole slide images. In: Proceedings of the IEEE/CVF international conference on computer vision. pp. 4015–4025 (2021)
10. Corso, G., Cavalleri, L., Beaini, D., Liò, P., Veličković, P.: Principal neighbourhood aggregation for graph nets. *Advances in neural information processing systems* **33**, 13260–13271 (2020)
11. Deng, J., Dong, W., Socher, R., Li, L.J., Li, K., Fei-Fei, L.: Imagenet: A large-scale hierarchical image database. In: 2009 IEEE conference on computer vision and pattern recognition. pp. 248–255. Ieee (2009)
12. Dietterich, T.G., Lathrop, R.H., Lozano-Pérez, T.: Solving the multiple instance problem with axis-parallel rectangles. *Artificial intelligence* **89**(1-2), 31–71 (1997)
13. Graham, S., Vu, Q.D., Raza, S.E.A., Azam, A., Tsang, Y.W., Kwak, J.T., Rajpoot, N.: Hover-net: Simultaneous segmentation and classification of nuclei in multi-tissue histology images. *Medical Image Analysis* **58**, 101563 (2019)
14. Gupta, R.K., Kurian, N.C., Jeevan, P., Sethi, A., et al.: Heterogeneous graphs model spatial relationships between biological entities for breast cancer diagnosis. *arXiv preprint arXiv:2307.08132* (2023)
15. Hanna, M.G., Parwani, A., Sirintrapun, S.J.: Whole slide imaging: technology and applications. *Advances in Anatomic Pathology* **27**(4), 251–259 (2020)
16. Hashimoto, N., Hanada, H., Miyoshi, H., Nagaishi, M., Sato, K., Hontani, H., Ohshima, K., Takeuchi, I.: Multimodal gated mixture of experts using whole slide image and flow cytometry for multiple instance learning classification of lymphoma. *Journal of Pathology Informatics* **15**, 100359 (2024)

17. He, K., Zhang, X., Ren, S., Sun, J.: Deep residual learning for image recognition. In: Proceedings of the IEEE conference on computer vision and pattern recognition. pp. 770–778 (2016)
18. Ilse, M., Tomczak, J., Welling, M.: Attention-based deep multiple instance learning. In: International conference on machine learning. pp. 2127–2136. PMLR (2018)
19. Jaume, G., Pati, P., Bozorgtabar, B., Foncubierta, A., Anniciello, A.M., Feroce, F., Rau, T., Thiran, J.P., Gabrani, M., Goksel, O.: Quantifying explainers of graph neural networks in computational pathology. In: Proceedings of the IEEE/CVF conference on computer vision and pattern recognition. pp. 8106–8116 (2021)
20. Javed, S.A., Juyal, D., Padigela, H., Taylor-Weiner, A., Yu, L., Prakash, A.: Additive mil: Intrinsically interpretable multiple instance learning for pathology. *Advances in Neural Information Processing Systems* **35**, 20689–20702 (2022)
21. Kingma, D.P., Ba, J.: Adam: A method for stochastic optimization. arXiv preprint arXiv:1412.6980 (2014)
22. Lou, W., Li, G., Wan, X., Li, H.: Cell graph transformer for nuclei classification. In: Proceedings of the AAAI Conference on Artificial Intelligence. vol. 38, pp. 3873–3881 (2024)
23. Maron, O., Lozano-Pérez, T.: A framework for multiple-instance learning. *Advances in neural information processing systems* **10** (1997)
24. Mobadersany, P., Yousefi, S., Amgad, M., Gutman, D.A., Barnholtz-Sloan, J.S., Velázquez Vega, J.E., Brat, D.J., Cooper, L.A.: Predicting cancer outcomes from histology and genomics using convolutional networks. *Proceedings of the National Academy of Sciences* **115**(13), E2970–E2979 (2018)
25. Nair, A., Arvidsson, H., Gatica V, J.E., Tudzarovski, N., Meinke, K., Sugars, R.V.: A graph neural network framework for mapping histological topology in oral mucosal tissue. *BMC bioinformatics* **23**(1), 506 (2022)
26. Nishiyama, D., Fukuchi, K., Akimoto, Y., Sakuma, J.: Camri loss: Improving recall of a specific class without sacrificing accuracy. In: 2022 International Joint Conference on Neural Networks (IJCNN). pp. 1–8. IEEE (2022)
27. Nishiyama, D., Fukuchi, K., Akimoto, Y., Sakuma, J.: Camri loss: Improving the recall of a specific class without sacrificing accuracy. *IEICE TRANSACTIONS on Information and Systems* **106**(4), 523–537 (2023)
28. Pati, P., Jaume, G., Foncubierta-Rodríguez, A., Feroce, F., Anniciello, A.M., Scognamiglio, G., Brancati, N., Fiche, M., Dubruc, E., Riccio, D., et al.: Hierarchical graph representations in digital pathology. *Medical image analysis* **75**, 102264 (2022)
29. Shao, Z., Bian, H., Chen, Y., Wang, Y., Zhang, J., Ji, X., et al.: Transmil: Transformer based correlated multiple instance learning for whole slide image classification. *Advances in Neural Information Processing Systems* **34**, 2136–2147 (2021)
30. Sims, J., Grabsch, H.I., Magee, D.: Using hierarchically connected nodes and multiple gnn message passing steps to increase the contextual information in cell-graph classification. In: MICCAI Workshop on Imaging Systems for GI Endoscopy. pp. 99–107. Springer (2022)
31. Song, A.H., Jaume, G., Williamson, D.F., Lu, M.Y., Vaidya, A., Miller, T.R., Mahmood, F.: Artificial intelligence for digital and computational pathology. *Nature Reviews Bioengineering* **1**(12), 930–949 (2023)
32. Wang, X., Peng, Y., Lu, L., Lu, Z., Bagheri, M., Summers, R.M.: Chestx-ray8: Hospital-scale chest x-ray database and benchmarks on weakly-supervised classification and localization of common thorax diseases. In: Proceedings of the IEEE conference on computer vision and pattern recognition. pp. 2097–2106 (2017)

33. Xu, K., Hu, W., Leskovec, J., Jegelka, S.: How powerful are graph neural networks? arXiv preprint arXiv:1810.00826 (2018)
34. Zhou, Y., Graham, S., Koohbanani, N.A., Shaban, M., Heng, P.A., Rajpoot, N.: Cgc-net: Cell graph convolutional network for grading of colorectal cancer histology images. In: The IEEE International Conference on Computer Vision (ICCV) Workshops (2019)